Inorganic Chemistry

Article

pubs.acs.org/IC

Experimental and Theoretical Investigations of Electronic Structure and Photoluminescence Properties of β-Ag_2MoO_4 Microcrystals

A. F. Gouveia,[†] J. C. Sczancoski,[‡] M. M. Ferrer,[†] A. S. Lima,[‡] M. R. M. C. Santos,[§] M. Siu Li,[∥] R. S. Santos,[⊥] E. Longo,[‡] and L. S. Cavalcante*[,⊥]

[†]LIEC-Universidade Federal de São Carlos, P.O. Box 676, 13565-905, São Carlos-SP, Brazil

[‡]Universidade Estadual Paulista, P.O. Box 355, 14801-907, Araraquara-SP, Brazil

[§]LIMAV-CCN-Materiais; UFPI, Universidade Federal do Piauí, 64049-550 Teresina-PI Brazil

[∥]IFSC-Universidade de São Paulo, P.O. Box 369, 13560-970, São Carlos, SP, Brazil

[⊥]Departamento de Química, UESPI, CCN, Rua João Cabral, P.O. Box 2231, 64002-150, Teresina-PI Brazil

Supporting Information

ABSTRACT: In this paper, we investigate a correlation between theoretical calculations and experimental data to explain the electronic structure and optical properties of silver molybdate (β-Ag_2MoO_4) microcrystals synthesized by the microwave-assisted hydrothermal method. X-ray diffraction, Rietveld refinement, and micro-Raman spectroscopy confirmed that these microcrystals crystallize in a spinel-type cubic structure. Field-emission scanning electron microscopy images revealed that the processing temperatures influence in the final shape of microcrystals. Optical properties were analyzed by ultraviolet−visible diffuse reflectance spectroscopy; the increase in the optical band gap energy (E_{gap}) (from 3.24 to 3.31 eV) with processing temperature is associated with the reduction of intermediary energy levels. First-principles quantum mechanical calculations based on the density functional theory at the B3LYP level were conducted. The calculated band structure revealed an indirect E_{gap} of approximately 4.00 and 3.34 eV for the β-Ag_2MoO_4 without and with the formation of defects, respectively. Theoretical calculations based on density of states and electron density maps were employed to understand the polarization phenomenon induced by structural defects in the β-Ag_2MoO_4 crystals. Finally, photoluminescence properties at room temperature of β-Ag_2MoO_4 microcrystals were explained by the charge-transfer mechanism involving tetrahedral [MoO_4] clusters.

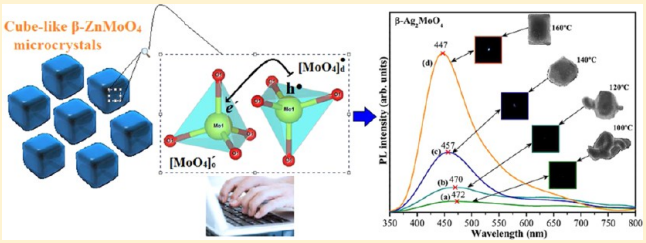

1. INTRODUCTION

Silver molybdate (Ag_2MoO_4) was commonly prepared by the oxide mixture or solid-state reaction,[1−3] melt-quenching technique,[4] and Czochralski growth.[5] However, these methods require high temperatures, long processing times, and/or sophisticated equipment. In addition, there is the possibility of the formation of a system composed of particles with nonhomogeneous sizes and irregular shapes as well as the appearing of deleterious phases. Recently, these disadvantages have been overcome by other synthetic methods.[6,7] The Ag_2MoO_4 phase is obtained by the following chemical routes: controlled precipitation,[8,9] conventional hydrothermal (CH) technique,[10,11] and microwave-assisted hydrothermal (MAH) method.[12] In particular, both CH and MAH techniques received special recognition in the literature because of their unique characteristics, such as the use of water as solvent, low processing temperatures (≤200 °C), and good control of particle sizes and shapes.[13−17] The hydrothermal method is defined as a chemical synthesis of inorganic materials performed in aqueous medium (with or without stabilizing agents) under temperature and pressure conditions.[18−21] In many cases, materials obtained by this chemical approach have a high degree of crystallinity, and it can be easily dispersed in other kinds of solvents.[21] Recently, the CH method was employed for the preparation of Ag_2MoO_4 and $Ag_2Mo_2O_7$ nanocrystals; however, long processing times (12−24 h) and elevated temperatures were required due to low reaction kinetics.[11,22,23]

Few reports in the literature have described Ag_2MoO_4 polymorphism. According to Arora et al.,[24] this oxide is able to exhibit a (α-phase) tetragonal structure or (β-phase) cubic structure, depending on the pressure used in the processing. Singh et al.[11] investigated the influence of pH on the formation of broom- and flowerlike Ag_2MoO_4 heterostructures by the CH approach. In another report, Fodjo et al.[25] used the borohydride reduction reaction to prepare Ag_2MoO_4 nanoparticles for applications in surface-enhanced Raman scattering activities. Also, published studies[12,26] have shown that Ag−Ag_2MoO_4 composites exhibit good photocatalytic activity under visible-light irradiation for the degradation of Rhodamine B as well as graphite/Ag_2MoO_4 lubricants in Ni-based composites to

Received: February 11, 2014
Published: May 20, 2014

   dx.doi.org/10.1021/ic500335x | Inorg. Chem. 2014, 53, 5589−5599

improve tribological properties, preventing the high-friction and wear.

Therefore, in this paper, we report on the synthesis of β-Ag_2MoO_4 microcrystals by the MAH method at different temperatures without the addition of surfactants. Structural characterizations were performed by X-ray diffraction (XRD), Rietveld refinement, and micro-Raman (M-Raman) spectroscopy. Morphological aspects were investigated by field-emission scanning electron microscopy (FE-SEM) images. Optical properties were focused on ultraviolet−visible (UV−vis) diffuse reflectance spectroscopy and photoluminescence (PL) properties at room temperature. The electronic band structure, density of states (DOS), and electron density maps of β-Ag_2MoO_4 crystals were theoretically calculated to understand the phenomenon of structural order−disorder on the electronic properties related to the PL emissions.

2. EXPERIMENTAL PROCEDURE

2.1. Synthesis of β-Ag_2MoO_4 Microcrystals by the MAH Method. The synthesis of β-Ag_2MoO_4 microcrystals is described as follows: 1×10^{-3} mol of molybdate sodium dihydrate ($Na_2MoO_4.2H_2O$; 99.5% purity, Sigma-Aldrich) and 2×10^{-3} mol of silver nitrate ($AgNO_3$; 99.8% purity, Sigma-Aldrich) were separately dissolved with deionized water contained in two plastic tubes (Falcon—capacity of 50 mL). These two solutions were then transferred into a Teflon autoclave (capacity of 150 mL), which was sealed and placed inside an adapted domestic microwave system. The MAH reactions were performed at different temperatures (100, 120, 140, and 160 °C) for 1 h. The temperature inside the autoclave was monitored using a CNT-120 temperature sensor (INCON Electronic Ltd., São Carlos-SP, Brazil). In principle, β-Ag_2MoO_4 microcrystals were obtained by the reaction between $2Ag^+$ and MoO_4^{2-} ions as described in eq 1:

$$2Na^+_{(aq)} + MoO^{2-}_{4(aq)} + 2H_2O + 2Ag^+_{(aq)} + 2NO^-_{3(aq)} \xrightarrow{\Delta T=100 \text{ to } 160^\circ C/1h} \beta\text{-}Ag_2MoO_{4(s)} + 2Na^+_{(aq)} + 2NO^-_{3(aq)} + 2H_2O \quad (1)$$

Finally, the resulting suspensions were washed with deionized water several times to remove any remaining Na^+ ions. Obtained precipitates (beige color) were collected and dried with acetone at room temperature for 8 h.

2.2. Characterizations of β-Ag_2MoO_4 Microcrystals. β-Ag_2MoO_4 microcrystals were structurally characterized by XRD patterns using a LabX XRD-6000 diffractometer (Shimadzu, Japan) with Cu Kα radiation (λ = 0.154 06 nm) in the 2θ range from 10° to 70° with a scanning velocity of 2°/min. Rietveld analysis was conducted in a 2θ range from 10° to 110° with a scanning velocity of 1°/min and a step of 0.02°. This structural refinement method has several advantages over conventional quantitative analysis methodologies, whole pattern-fitting algorithms are used, so all lines for each phase are explicitly considered, and even severely overlapped lines are usually not a problem.[27] The structural refinement was performed using the Maud program version 2.33,[28] which revealed the Rietveld texture and stress analysis.[29] The structural refinement quality is generally checked by R values (R_{wnb}, R_b, R_{exp}, R_w, and σ). The difference between observed and calculated patterns is the best way to judge the success of Rietveld refinement,[30] and other parameters with additional functions were applied to find a structural refinement with better quality and reliability. Optimized parameters were scale factor, background with the exponential shift, exponential thermal shift and polynomial coefficients, basic phase, microstructure, crystal structure, size strain (anisotropic, no rules), structure solution model (genetic algorithm SDPD), shift lattice constants, profile half-width parameters (u, v, w), texture, lattice parameters (a, b, c), factor occupancy, and atomic site occupancy (Wyckoff). Micro-Raman spectra were recorded using a SENTERRA spectrometer (Bruker, Germany) equipped with He−Ne laser (λ = 785 nm) and CCD operating from 25 to 1000 cm^{-1}. The incident laser beam power on the sample was kept at 6 mW. For the region located between 85 and 1000 cm^{-1}, 100 scans were completed with spectral resolution of 4 cm^{-1}. A 50 μm lens was used to prevent overheating of the sample. Morphological aspects of the microcrystals were verified with FE-SEM using an Inspect F50 microscope (FEICompany, Netherlands) operated at 15 kV. UV−vis spectra were taken using a Cary 5G spectrophotometer (Varian, USA) in diffuse-reflectance mode. PL measurements at room temperature were performed through a Monospec 27 monochromator (Thermal Jarrel Ash, USA) coupled to a R446 photomultiplier (Hamamatsu Photonics, Japan). A krypton-ion laser (Coherent Innova 90K, λ = 350 nm) was used as the excitation source; its maximum output power was maintained at 500 mW. The laser beam passed through an optical chopper so that the maximum power focused on the sample was kept at 40 mW.

2.3. Computational Method and Models for β-Ag_2MoO_4 Microcrystals. All theoretical calculations for β-Ag_2MoO_4 microcrystals were performed using a periodic approximation implemented in the CRYSTAL09 computer code.[31] The computational method is based on density functional theory (DFT) in conjunction with Becke's three-parameter hybrid nonlocal exchange functional[32] combined with the Lee−Yang−Parr gradient-corrected correlation functional, B3LYP.[33] Ag and Mo atomic centers are described by basis sets PS-311d31G and PS-311(d31)G, which were taken from the Crystal Web site[34] where PS stands for Hay and Wadt's nonrelativistic small core pseudopotential.[35] The O atom center is described by 8−411G taken from Mike Towler's Crystal Web site.[36] The diagonalization of the Fock matrix was performed at adequate k-point grids in the reciprocal space, which is the Pack−Monkhorst/Gilat shrinking factor IS = ISP = 4. Thresholds controlling the accuracy of the Coulomb and exchange integral calculations were set to 10^{-8} (ITOL1 to ITOL4) and 10^{-14} (ITOL5) which assures a convergence in total energy better than 10^{-7} a.u., whereas the percentage of the Fock/Kohn−Sham matrix mixing was set to 40 (IPMIX = 40).[31] Full optimization of (a, b, c) lattice parameters as well as (x, y, z) internal coordinates was conducted. The band structure diagram and DOS were carried out with CRYSTAL09.[31] Raman vibrational modes and their corresponding frequencies were calculated using numerical second derivatives of total energies as implemented in the CRYSTAL09 package.[31] Four models were constructed to more accurately describe structural and electronic properties derived from the experimental synthesis, an optimized bulk (β-Ag_2MoO_4_opt), and three models with displacements of Ag atoms (β-Ag_2MoO_4_Ag), Mo atoms (β-Ag_2MoO_4_Mo), and Ag/Mo atoms (β-Ag_2MoO_4_Ag/Mo).

3. RESULTS AND DISCUSSION

3.1. XRD: A Structural Order at Long-Range of β-Ag_2MoO_4 Microcrystals. The degree of structural order−disorder at long-range or periodicity of β-Ag_2MoO_4 microcrystal was verified by the XRD technique. Figure 1a−d illustrates the XRD patterns of β-Ag_2MoO_4 microcrystals prepared at different temperatures for 1 h by the MAH method.

XRD patterns in Figure 1a−d indicated that all β-Ag_2MoO_4 microcrystals have a spinel-type cubic structure with space group ($Fd\bar{3}m$) and point-group symmetry (O_h^7).[37,38] These crystals have sharp and well-defined diffraction peaks, indicating a good degree of structural order at long-range. However, it is difficult to identify any Ag^0 in these crystals by the XRD measurements.[39] In addition, respective positions of all diffraction peaks in these XRD diffractograms are in good agreement with the results reported in the Inorganic Crystal Structure Data (ICSD) base No. 36187[37] and in the literature.[40−42]

3.2. Rietveld Refinement of β-Ag_2MoO_4 Microcrystals. Structural refinements using the Rietveld method[43] confirmed that all β-Ag_2MoO_4 microcrystals have a spinel-type cubic structure without secondary phases (see Figure 2 and Supporting Information, Figure S1a−c).

Rietveld refinement was based on the β-Ag_2MoO_4 phase with spinel-type cubic structure described in the Crystallographic

dx.doi.org/10.1021/ic500335x | Inorg. Chem. 2014, 53, 5589−5599

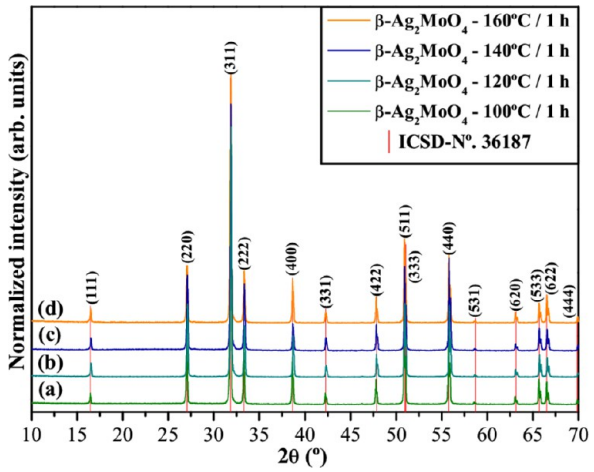

Figure 1. XRD patterns for β-Ag_2MoO_4 microcrystals processed at different temperatures: (a) 100 °C, (b) 120 °C, (c) 140 °C, (d) 160 °C for 1 h. The vertical red lines indicate the position and relative intensity of the respective ICSD Card No. 36187.

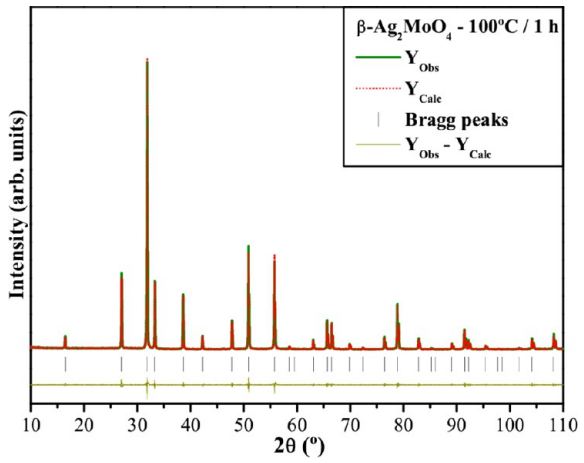

Figure 2. Rietveld refinement plot for β-Ag_2MoO_4 microcrystals processed at 100 °C for 1 h.

Information File (CIF) No. 36187.[37] All structural refinements (Figure 2 and Supporting Information, Figure S1a–c) showed good correlation between observed and calculated XRD patterns ($Y_{Obs} - Y_{Calc}$ lines), indicating the reliability of the results. More details on these obtained data are displayed in Table 1 and Supporting Information, Table S1.

In these tables, fit parameters (R_{wnb}, R_b, R_{exp}, R_w, and σ) suggest that refinement results are very reliable. There are considerable variations in the atomic positions related to the oxygen (O) atoms, while the silver (Ag) atoms and molybdenum (Mo) atoms remain fixed in their positions into the cubic structure. This information suggests the existence of structural distortions on octahedral [AgO_6] and tetrahedral [MoO_4] clusters belonging to the β-Ag_2MoO_4 cubic structure, which arise from coupling with microwaves. Lattice parameters and the internal coordination estimated from the optimized structure (theoretical model) and refined parameters are listed in Table 1.

3.3. Unit Cell Representation of β-Ag_2MoO_4. Figure 3 shows a schematic representation of a β-Ag_2MoO_4 structure modeled from Rietveld refinement data.

Lattice parameters and atomic positions obtained from Rietveld refinements were used to model this structure by the

Table 1. Lattice Parameters, Unit Cell Volume, and Atomic Coordinate Obtained Experimentally from the Structural Refinement by the Rietveld Method for β-Ag_2MoO_4 Microcrystals Processed at 100°C for 1 h and Theoretically Calculated from DFT Method for β-Ag_2MoO_4 Crystals

atoms[a]	Wyckoff[b]	site[c]	x	y	z
Ag	16d	.−3m	0.625	0.625	0.625
Mo	8a	−43m	0	0	0
O	32e	.3m	0.3524	0.3524	0.3524
atoms[d]	Wyckoff	site[e]	x	y	z
Ag	16d	.−3m	0.625	0.625	0.625
Mo	8a	−43m	0	0	0
O	32e	.3m	0.36	0.36	0.36

[a] $a = b = c = 9.317(9)$ Å; $V = 809.0(1)$ Å^3; $Z = 8$ [b] $R_w = 10.34\%$; $R_{wnb} = 10.01\%$; $R_b = 7.9\%$; $R_{exp} = 7.3\%$ and $\sigma = 1.41$ [c] β-Ag_2MoO_4 microcrystals obtained at 100 °C for 1 h by the MAH method [d] $a = b = c = 9.318(5)$ Å; $V = 809.1(7)$ Å^3; $Z = 8$ [e] β-Ag_2MoO_4 crystals (theoretical DFT method)

Visualization for Electronic and Structural Analysis (VESTA) program (version 3.1.8 for Windows).[44] The spinel-type cubic structure of β-Ag_2MoO_4 microcrystals is characterized by the space group ($Fd\bar{3}m$) with eight molecular formula per unit cell ($Z = 8$).[37] In these structures, Ag atoms are coordinated to six O atoms, forming distorted octahedral [AgO_6] clusters. Basically, these polyhedra have a symmetry group (O_h) with six vertices, eight faces, and 12 edges (see Figure 3).[45] In this same figure, Mo atoms are coordinated to four O atoms, resulting in tetrahedral [MoO_4] clusters. In this case, these tetrahedra are related to the T_d symmetry group with four vertices, four faces, and six edges.[46] These [MoO_4] clusters are slightly distorted in the lattice and exhibit a particular characteristic related to differences in O–Mo–O bond angles. In principle, we presume that experimental conditions employed in the synthesis as well as the influence of the microwave radiation during processing were key factors to cause local distortions in both octahedral [AgO_6] and tetrahedral [MoO_4] clusters.

3.4. M-Raman Spectroscopy Analyses of β-Ag_2MoO_4. β-Ag_2MoO_4 microcrystals obtained in this study exhibit a spinel-type cubic structure with a space group ($Fd\bar{3}m$), a point-group symmetry (O_h^7), and eight molecules per unit cell ($Z = 8$).[37] Therefore, the total irreducible representation of vibrational modes or optical phonons is shown in Brillouin zone points as described by eq 2:[47]

$$\Gamma_{\{(\text{Raman})+[\text{Infravermelho}]\}} = (A_{1g} + E_g + 3T_{2g} + T_{1g}) + [4T_{1u} + 2A_{2u} + 2E_u + 2T_{2u}] \quad (2)$$

where A_g, E_g, and T_{2g} are Raman-active modes, while the T_{1g} mode has low intensity or is considered inactive. T_{1u} modes are detectable in IR spectra, and the other [$2A_{1u} + 2E_u + 2T_{2u}$] modes are inactive. The subscripted "g" and "u" terms indicate that the β-Ag_2MoO_4 phase has a centrosymmetric inversion. Therefore, only five active vibrational modes in M-Raman spectra are expected for β-Ag_2MoO_4 crystals, as represented by eq 3:

$$\Gamma_{(\text{Raman})} = A_{1g} + E_g + 3T_{2g} \quad (3)$$

Figure 4 illustrates the M-Raman spectra of β-Ag_2MoO_4 microcrystals prepared at different temperatures for 1 h by the MAH method.

dx.doi.org/10.1021/ic500335x | Inorg. Chem. 2014, 53, 5589–5599

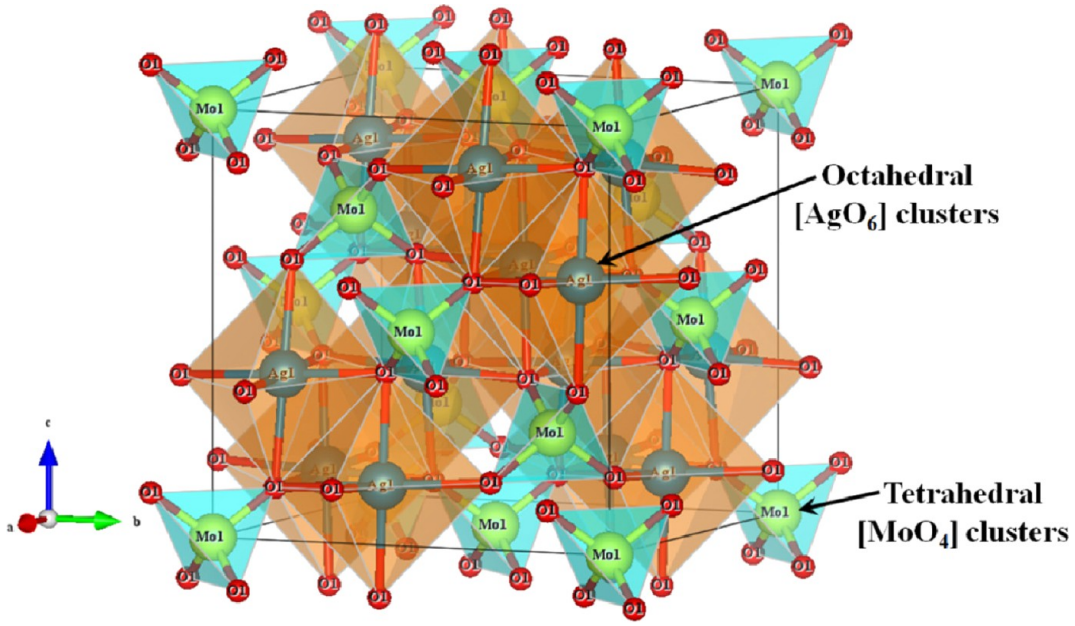

Figure 3. Schematic representation of the cubic unit cells corresponding to β-Ag_2MoO_4 crystals.

In these spectra were detected four Raman-active modes located between 85 and 1000 cm^{-1}. All these modes are intense and well-defined,

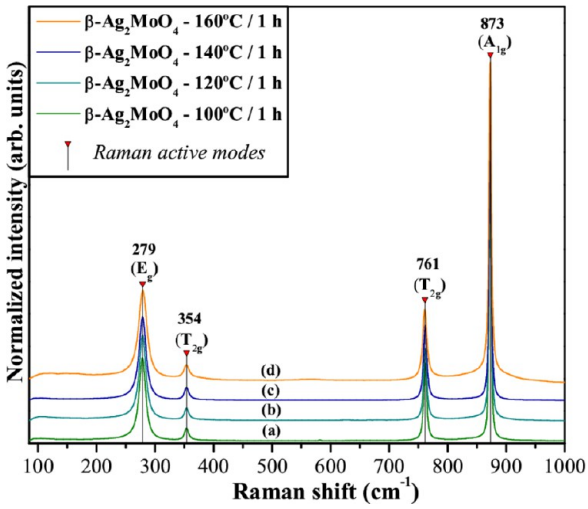

Figure 4. Micro-Raman spectra of β-Ag_2MoO_4 microcrystals processed at different temperatures: (a) 100 °C, (b) 120 °C, (c) 140 °C, (d) 160 °C for 1 h. The vertical lines indicate the positions and relative intensities of experimental Raman-active modes.

suggesting that all β-Ag_2MoO_4 microcrystals are structurally ordered at short range. The E_g mode located at 279 cm^{-1} is due to external structure vibrations of octahedral [AgO_6] clusters, while two T_{2g} modes found at 354 and 761 cm^{-1} are related to torsional vibrations of O−Mo−O bonds inside tetrahedral [MoO_4] clusters. The A_{1g} mode situated at 873 cm^{-1} is caused by symmetric stretching vibrations of [← O←Mo → O→] bonds.[48] However, one T_{2g} mode related to the mobility of O atoms into the cubic structure was not experimentally detectable. Particularly, it is possible to conclude that this mode exhibits a lower intensity in these spectra. On the other hand, theoretical calculations reported in the literature[47] have provided the existence of this Raman-active mode.

Relative experimental and theoretical positions of these vibrational modes are displayed in Table 2 and Figure 5. This figure confirms the good agreement between experimental and theoretical Raman modes of β-Ag_2MoO_4 microcrystals with the literature.[11,24,47,48]

3.5. FE-SEM Analyses of β-Ag_2MoO_4 Microcrystals.

Figure 6a−h illustrates FE-SEM images of β-Ag_2MoO_4 microcrystals prepared at different temperatures for 1 h by the MAH method.

In the initial stage, the aqueous solution at room temperature rapidly solvates Ag^+ and MoO_4^{2-} ions. The partial negative charge of H_2O molecules is electrostatically attracted by Ag^+ ions, while the other partial positive charge of these molecules is

Table 2. Relative Positions of Active Raman Modes (Experimental and Theoretical)

	M[a]	CH[b]	PC[c]	THEO[d]	CH	MAH[e]	MAH[e]	MAH[e]	MAH[e]	THEO[d]
	T^f (°C)	150	300		140	100	120	140	160	
	t^g (h)	12	5		12	1	1	1	1	
	T_{2g}			89						93
	E_g	281	278	279	278	279	279	279	279	272
Raman	T_{2g}	355	352	367	354	354	354	354	354	370
active	T_{2g}	764	761	790	764	761	761	761	761	776
modes[h]	A_{1g}	874	873	895	873	873	873	873	873	867
	ref.	11	24	47	48	¶[i]	¶[i]	¶[i]	¶[i]	¶[i]

[a]M = method. [b]CH = conventional hydrothermal. [c]PC = precipitation and calcination. [d]THEO = theoretical. [e]MAH = microwave-assisted hydrothermal. [f]T = temperature. [g]t = time. [h]Active Raman modes = (cm^{-1}). [i]¶ = this work.

dx.doi.org/10.1021/ic500335x | Inorg. Chem. 2014, 53, 5589−5599

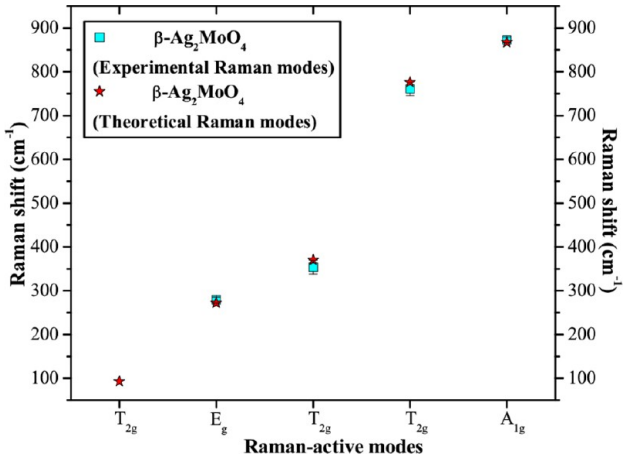

Figure 5. Comparison between relative positions of theoretical and experimental Raman-active modes for β-Ag_2MoO_4 microcrystals.

attracted by MoO_4^{2-} ions.[49] However, due to differences in the electronic density between Ag^+ and MoO_4^{2-} ions, a strong electrostatic attraction occurs between these ions, which results in the formation of first β-Ag_2MoO_4 precipitates or nucleation seeds.[50] In MAH processing stages at 100 °C for 1 h, the microwave radiation is able to promote localized superheating in the aqueous solution as well as accelerate solid particles to high velocities. These two phenomena induce a random aggregation among the small particles due to the increase of effective collisions, inducing the formation of a system composed of several irregular β-Ag_2MoO_4 microcrystals (see Figure 6a,b). Figure 6c–f confirms a mass transport among the particles in contact at temperatures of 120 and 140 °C. As a consequence of this mechanism, the formation of particles with well-defined shapes is impossible. Despite the polydisperse nature, ideal thermodynamic conditions for the anisotropic growth of cube-shaped particles were found at 160 °C (see Figure 6g,h). Therefore, these observations clearly indicate that the processing temperature is a key parameter in the morphologic control of β-Ag_2MoO_4 microcrystals. Recently, Li et al.[12] reported the formation of this same cubelike microstructure for Ag–Ag_2MoO_4 composites synthesized by the MAH method. According to these authors, in addition to the polyvinylpyrrolidone concentration, both the reaction temperature and time are crucial parameters for the crystal growth and final shape of these oxides.

3.6. UV–vis Diffuse Reflectance Spectroscopy and Band Structures of β-Ag_2MoO_4 Microcrystals. The optical band gap energy (E_{gap}) was calculated by the Kubelka–Munk equation,[51] which is based on the transformation of diffuse reflectance measurements to estimate E_{gap} values with good accuracy.[52] Particularly, it is used in limited cases of infinitely thick samples. The Kubelka–Munk eq 4 for any wavelength is described by

$$F(R_\infty) = \frac{(1 - R_\infty)^2}{2R_\infty} = \frac{k}{s} \quad (4)$$

where $F(R_\infty)$ is the Kubelka–Munk function or absolute reflectance of the sample. In our case, magnesium oxide (MgO) was adopted as the standard sample in reflectance measurements; $R_\infty = R_{sample}/R_{MgO}$ (R_∞ is the reflectance), k is the molar absorption coefficient, and s is the scattering coefficient. In a parabolic band structure, the optical band gap and absorption coefficient of semiconductor oxides[53] can be calculated by eq 5:

$$\alpha h\nu = C_1(h\nu - E_{gap})^n \quad (5)$$

where α is the linear absorption coefficient of the material, $h\nu$ is the photon energy, C_1 is a proportionality constant, E_{gap} is the optical band gap, and n is a constant associated with different kinds of electronic transitions ($n = 1/2$ for a direct allowed, $n = 2$ for an indirect allowed, $n = 1.5$ for a direct forbidden, and $n = 3$ for an indirect forbidden). According to the theoretical calculations, β-Ag_2MoO_4 microcrystals exhibit an optical absorption spectrum governed by indirect electronic transitions. In this phenomenon, after the electronic absorption process, electrons located in minimum energy states in the conduction band (CB) are able to go back to maximum energy states of the valence band (VB) in distinct points in the Brillouin zone.[54] On the basis of this information, E_{gap} values of β-Ag_2MoO_4 microcrystals were calculated using $n = 2$ in eq 5. Finally, using the absolute reflectance function described in eq 6 with $k = 2\alpha$, we obtain the modified Kubelka–Munk equation as indicated in eq 6:

$$[F(R_\infty)h\nu)^{1/2} = C_2(h\nu - E_{gap}) \quad (6)$$

Therefore, finding the $F(R_\infty)$ value from eq 6 and plotting a graph of $[F(R_\infty)h\nu]^{1/2}$ against $h\nu$, E_{gap} values were calculated for β-Ag_2MoO_4 microcrystals by extrapolating the linear portion of UV–vis curves.

Figure 7a–d shows UV–vis spectra of β-Ag_2MoO_4 microcrystals prepared at different temperatures by the MAH method; Figure 7e–h illustrates band structures of β-Ag_2MoO_4_opt, β-Ag_2MoO_4_Ag, β-Ag_2MoO_4_Mo, and β-Ag_2MoO_4_Ag/Mo by displacements of 0.25 Å along the z-axis, respectively.

Figure 7a–d shows a slight increase in the E_{gap} with an increase in the processing temperature. In principle, we believe that this behavior is related to a reduction in intermediary energy levels between the VB and CB, since the exponential optical absorption edge and E_{gap} are controlled by the degree of structural order–disorder in the lattice.[55] We attribute the presence of these two absorption regions to the inhomogeneous shapes of β-Ag_2MoO_4 microcrystals obtained at different temperatures by the MAH method. However, when the processing was performed at 160 °C, the majority of the microcrystals in this system presented a cubelike shape. In this study it is not possible to calculate the average crystal size because of the irregular morphologies of the crystals at low temperatures. The decrease in E_{gap} values can be attributed to structural defects at medium-range and local bond distortions, yielding localized electronic levels within the forbidden band gap. A smaller E_{gap} was detected for β-Ag_2MoO_4 microcrystals processed at 100 °C for 1 h (see Figure 7a), which suggests a high concentration of defects in the lattice. However, the existence of electronic levels in these crystals can be achieved only by theoretical calculations, as illustrated in Figure 7e–h. Theoretical studies of the E_{gap} were carried out using different displacements for the β-Ag_2MoO_4_Ag, β-Ag_2MoO_4_Mo, and β-Ag_2MoO_4_Ag/Mo models (see Table 3). Band structures of all β-Ag_2MoO_4 are typically characterized by well-defined indirect electronic transitions, as verified in our theoretical calculations. A primitive cubic Brillouin zone with representations of the paths is presented in the Supporting Information (Figure S2); in the band structures of β-Ag_2MoO_4_opt and β-Ag_2MoO_4_Ag, the top of the VB is located at the Γ (0, 0, 0) point, and the bottom of the CB is placed at the X (1/2, 0, 1/2) point; β-Ag_2MoO_4_Mo and β-Ag_2MoO_4_Ag/Mo models exhibited a new configuration for the CB structure. The indirect characteristic of the band gap was retained, although the kind of indirect transition is altered

dx.doi.org/10.1021/ic500335x | Inorg. Chem. 2014, 53, 5589–5599

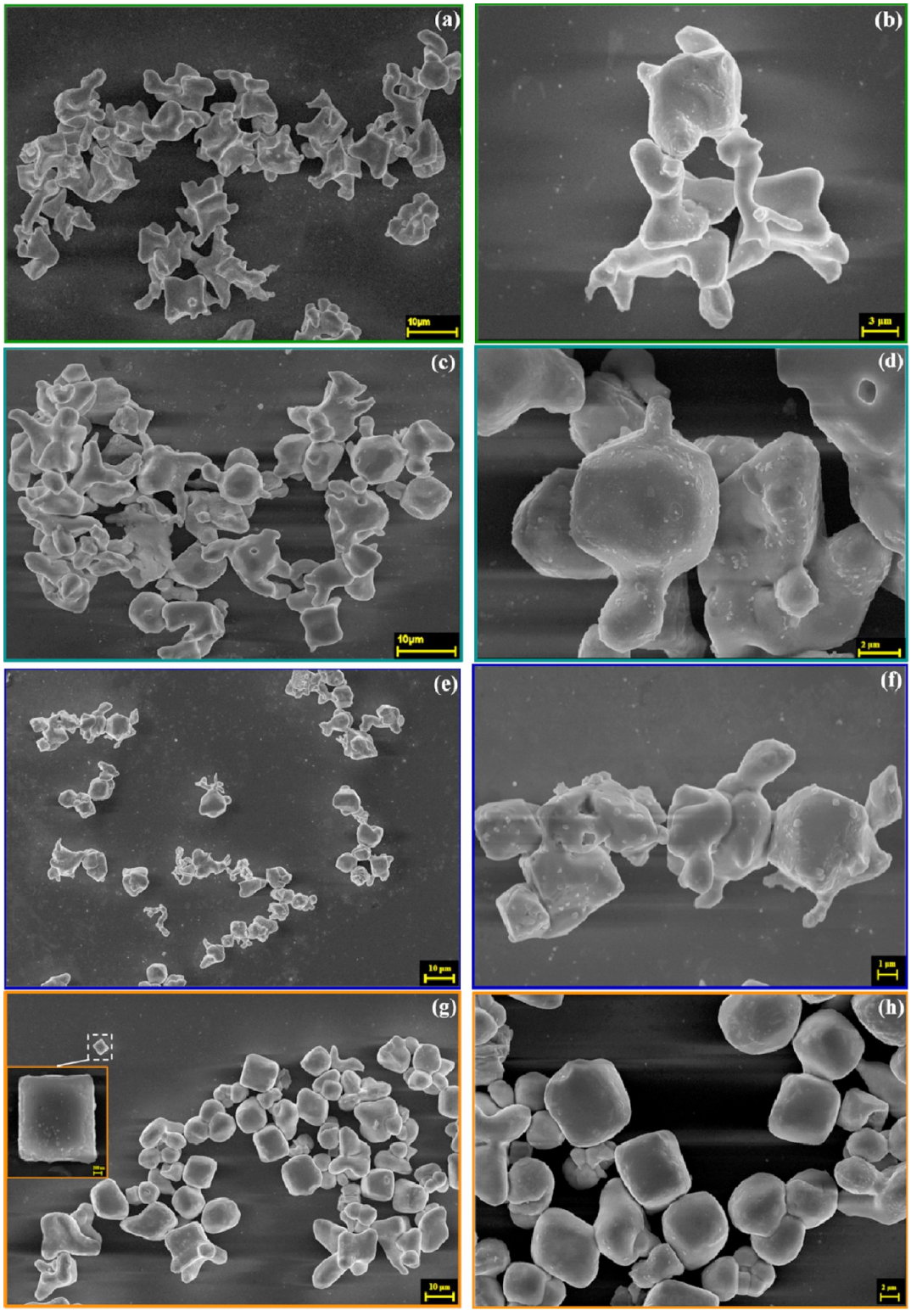

Figure 6. FE-SEM images for β-Ag_2MoO_4 microcrystals processed at different temperatures. (a) 100 °C (low magnification). (b) 100 °C (high magnification). (c) 120 °C (low magnification). (d) 120 °C (high magnification). (e) 140 °C (low magnification). (f) 140 °C (high magnification). (g) 160 °C (low magnification). (inset) An individual cubelike β-Ag_2MoO_4 microcrystal. (h) 160 °C (high magnification).

from $\Gamma-X$ to $\Gamma-W$, where *W is* the (1/2, 1/4, 3/4) point. The displacement of Mo causes a decreasing of the band gap in relation to displacements performed on Ag atoms. In this structure, Mo atoms are network former clusters with a strong covalent hybridization between 2p orbitals, which refers to O atoms in VB and 4d orbitals of Mo atoms in the CB. The perturbation in tetrahedral $[MoO_4]$ clusters creates new intermediate levels in the forbidden region, promoting different electronic transitions and decreasing the E_{gap} (see Table 3).

The average defect densities into the lattice of molybdates can be related to intermediary levels formed between the VB and CB at medium range. In Table 3, bond distances between Mo−O and

dx.doi.org/10.1021/ic500335x | *Inorg. Chem.* 2014, 53, 5589−5599

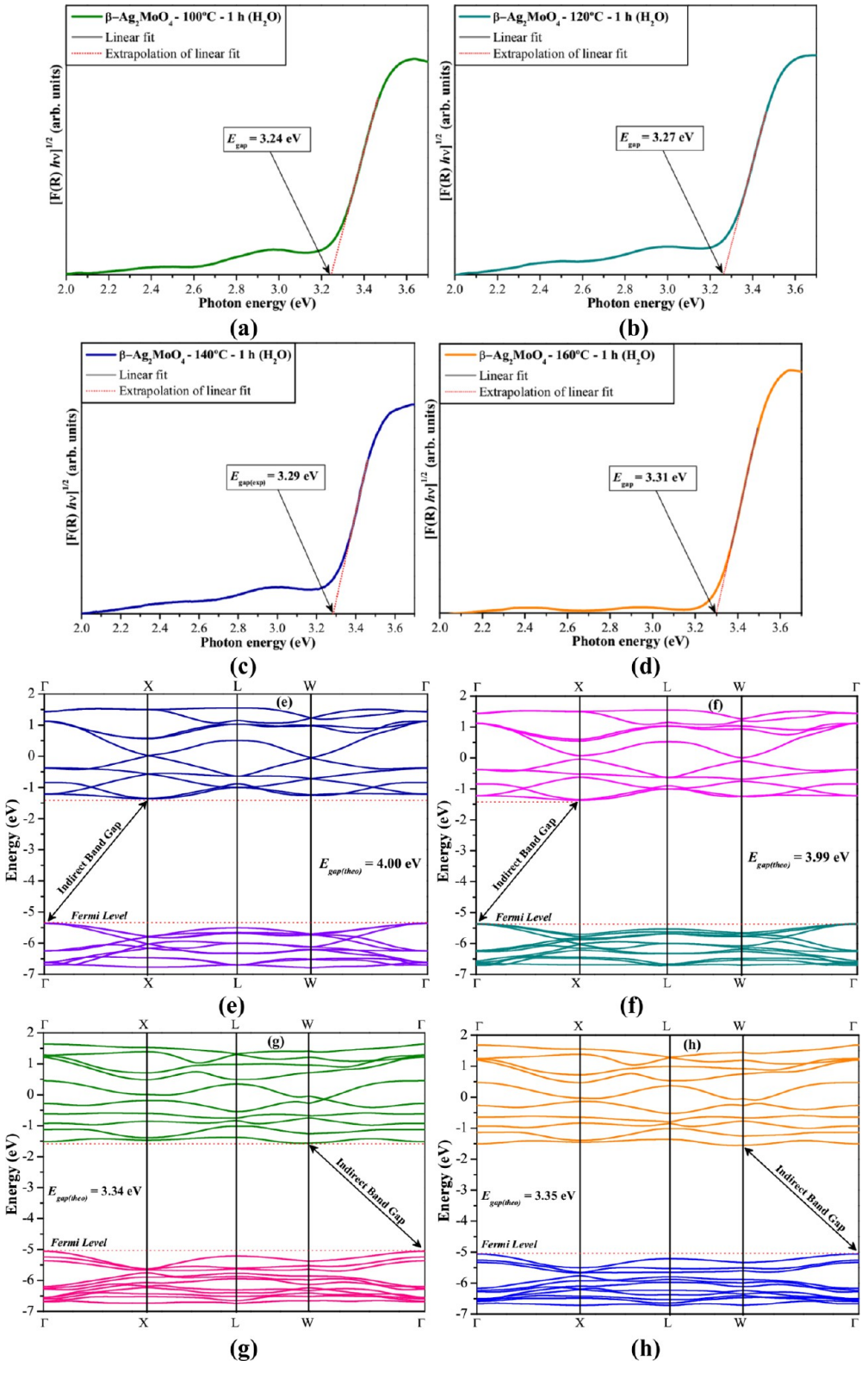

Figure 7. UV–vis spectra for β-Ag_2MoO_4 microcrystals processed at different temperatures: (a) 100 °C, (b) 120 °C, (c) 140 °C, (d) 160 °C for 1 h. BAND structures for: (e) bulk-optimized β-Ag_2MoO_4 crystals, and displacements of 0.25 Å in the (f) Ag atoms of β-Ag_2MoO_4 crystals, (g) Mo atoms of β-Ag_2MoO_4 crystals, and (h) Ag/Mo atoms of β-Ag_2MoO_4 crystals.

Ag–O bonds were modified to build a theoretical model to better describe the experimental E_{gap} of β-Ag_2MoO_4 microcrystals. This model is the key point in understanding the effects of structural order–disorder, especially those arising from distortions in Mo–O bonds on the electronic properties of β-Ag_2MoO_4 microcrystals. Our theoretical data calculated with the displacement of 0.25 Å in Mo–O bonds is reflected in the good correlation between experimental and theoretical E_{gap} results. This displacement promoted a symmetry break, causing the polarization of the structure by the formation of holes ($h^{\bullet}$) - electrons (e') within the forbidden region.

dx.doi.org/10.1021/ic500335x | Inorg. Chem. 2014, 53, 5589–5599

Table 3. Optical Band Gap Values (Theoretical) For Optimized Structure and Displacements of Atoms

model	displacement (Å)	E_{gap} (eV)
β-Ag_2MoO_4_opt	0.00	4.00
β-Ag_2MoO_4_Ag	0.05	4.00
	0.10	4.00
	0.15	3.99
	0.20	3.99
	0.25	3.99
β-Ag_2MoO_4_Mo	0.05	3.93
	0.10	3.82
	0.15	3.69
	0.20	3.52
	0.25	3.34
β-Ag_2MoO_4_Ag/Mo	0.05	3.93
	0.10	3.82
	0.15	3.69
	0.20	3.53
	0.25	3.35

3.7. DOS and Electron Density Maps of β-Ag_2MoO_4 Microcrystals. Figure 8a,b shows DOS for β-Ag_2MoO_4_opt (without displacement) and β-Ag_2MoO_4_Mo (displacement of 0.25 Å performed on the Mo atom in *z*-axis), respectively.

In both models, the projected DOS indicates that the VB is mainly composed of Ag 4d ($4d_{z^2} + 4d_{x^2-y^2}$; $4d_{xz} + 4d_{yz} + 4d_{xy}$) and O 2p ($2p_x + 2p_y + 2p_z$) orbitals, while the CB is predominantly formed of Mo 4d ($4d_{z^2} + 4d_{x^2-y^2}$; $4d_{xz} + 4d_{yz} + 4d_{xy}$) orbitals. In contrast, after the displacement of 0.25 Å on the Mo atom, there is a small contribution of Ag 6s orbitals in the CB. The DOS of both β-Ag_2MoO_4_Ag and β-Ag_2MoO_4_Ag/Mo models are reported in Supporting Information (see Figure S3a,b).

Figure 9a–d shows DOS projections for the β-Ag_2MoO_4_opt and β-Ag_2MoO_4_Mo models, making it possible to analyze the influence of tetragonal [MoO_4] clusters into the cubic structure.

According to theoretical calculations, the β-Ag_2MoO_4_opt model has two kinds of $[MoO_4]_o^x$ and $[MoO_4]_d^x$ clusters, where the subscript "o" is ordered, "d" is disordered/distorted, and "*x*" is neutral or very similar (see Figure 9a,b). In this specific case, it is possible to identify that the VB has only the participation of O 2p ($2p_x + 2p_y + 2p_z$) orbitals; however, in relation to the CB, there is a higher contribution of Mo $4d_{xz} + 4d_{yz}$ orbitals. When a defect in the structure (β-Ag_2MoO_4_Mo model) was caused by the atomic displacement of 0.25 Å on the Mo atom, two new kinds ($[MoO_4]_o'$ and $[MoO_4]_d^\bullet$) of clusters were observed, in which the subscript is the cluster with one electron, and $^\bullet$ is the cluster with one hole (see Figure 9c,d). Therefore, the DOS revealed that the VB has a predominance of O 2p orbitals. Contrary to the β-Ag_2MoO_4_opt model, the CB involves a higher number of Mo $4d_{z^2}$ orbitals than $4d_{xz} + 4d_{yz}$ orbitals (see Figure 9c,d). Thus, the calculations indicate an E_{gap} of 4.00 eV for the β-Ag_2MoO_4_opt and 3.34 eV for the β-Ag_2MoO_4_Mo. This information suggests that the existence of structural defects induces the appearance of intermediary energy levels within the forbidden region and reduces the E_{gap} of β-Ag_2MoO_4 microcrystals.

Figure 10a,b shows two-dimensional electron density maps with a view of the (101) plane in β-Ag_2MoO_4_opt and β-Ag_2MoO_4_Mo models, respectively.

Initially, this figure displayed a color scale on each map, demonstrating zones with high and low electronic densities.[56] The more positive scale has the higher electronic density in a given region and vice versa. Thus, in these two β-Ag_2MoO_4_opt and β-Ag_2MoO_4_Mo models, the areas in white color exhibit a high electronic density, while those in dark blue color demonstrate the absence of electronic charge. This selected plane facilitates a clear identity of the cross section of three [MoO_4] clusters in both models. The covalent interaction of O with Mo atoms is visible in light blue areas with elliptical geometry. For the β-Ag_2MoO_4_opt, there is a similarity between electronic distributions of $[MoO_4]_o^x$ and $[MoO_4]_d^x$ clusters due to the slight equivalency of Mo–O bond distances (see Figure 10a). In contrast, for the β-Ag_2MoO_4_Mo model, the perturbation in the system by the displacement of 0.25 Å on the Mo atom resulted in an inhomogeneous electron distribution on [MoO_4] clusters (referred to as $[MoO_4]_d^\bullet$), which resulted in the formation of $h^\bullet$ (see Figure 10b). This defect in a cluster generates polarization in the structure, as a consequence of the charge transfer from perturbed ($[MoO_4]_d^\bullet$) to unperturbed ($[MoO_4]_o'$) clusters (formation of $e'-h^\bullet$ pairs).

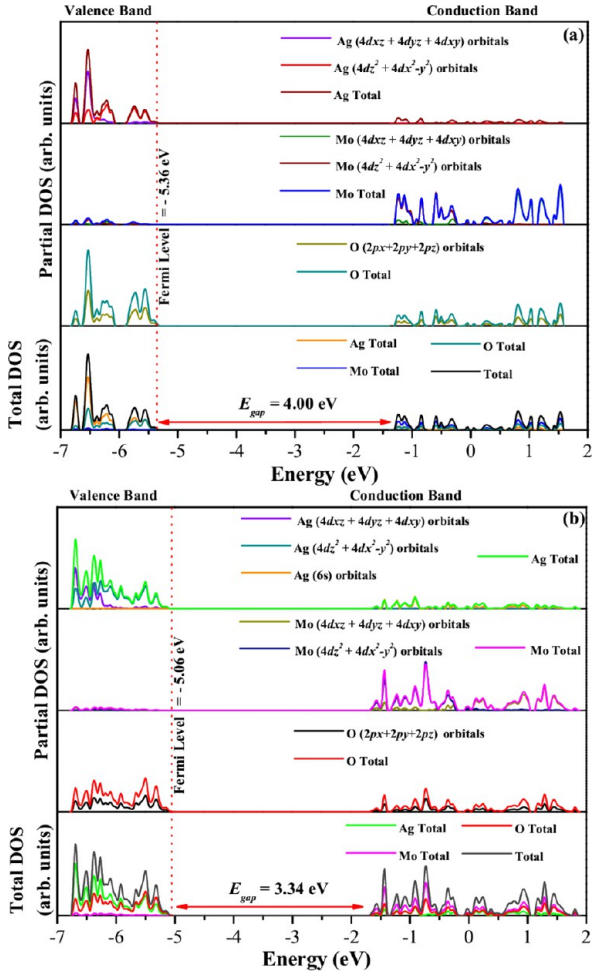

Figure 8. Partial and total DOS for (a) bulk-optimized β-Ag_2MoO_4 crystals optimized model and (b) displacements of 0.25 Å in the Mo atoms of β-Ag_2MoO_4 crystals.

3.8. PL Spectra of β-Ag_2MoO_4 Microcrystals. Figure 11a–d illustrates the PL spectra at room temperature of β-Ag_2MoO_4 microcrystals.

According to the literature,[37] PL properties of Ag_2MoO_4 crystals are related to microstructural changes and aggregation effects. In addition, morphological aspects are able to dislocate crystal lattice planes as well as adjacent particles in aggregates,

dx.doi.org/10.1021/ic500335x | Inorg. Chem. 2014, 53, 5589–5599

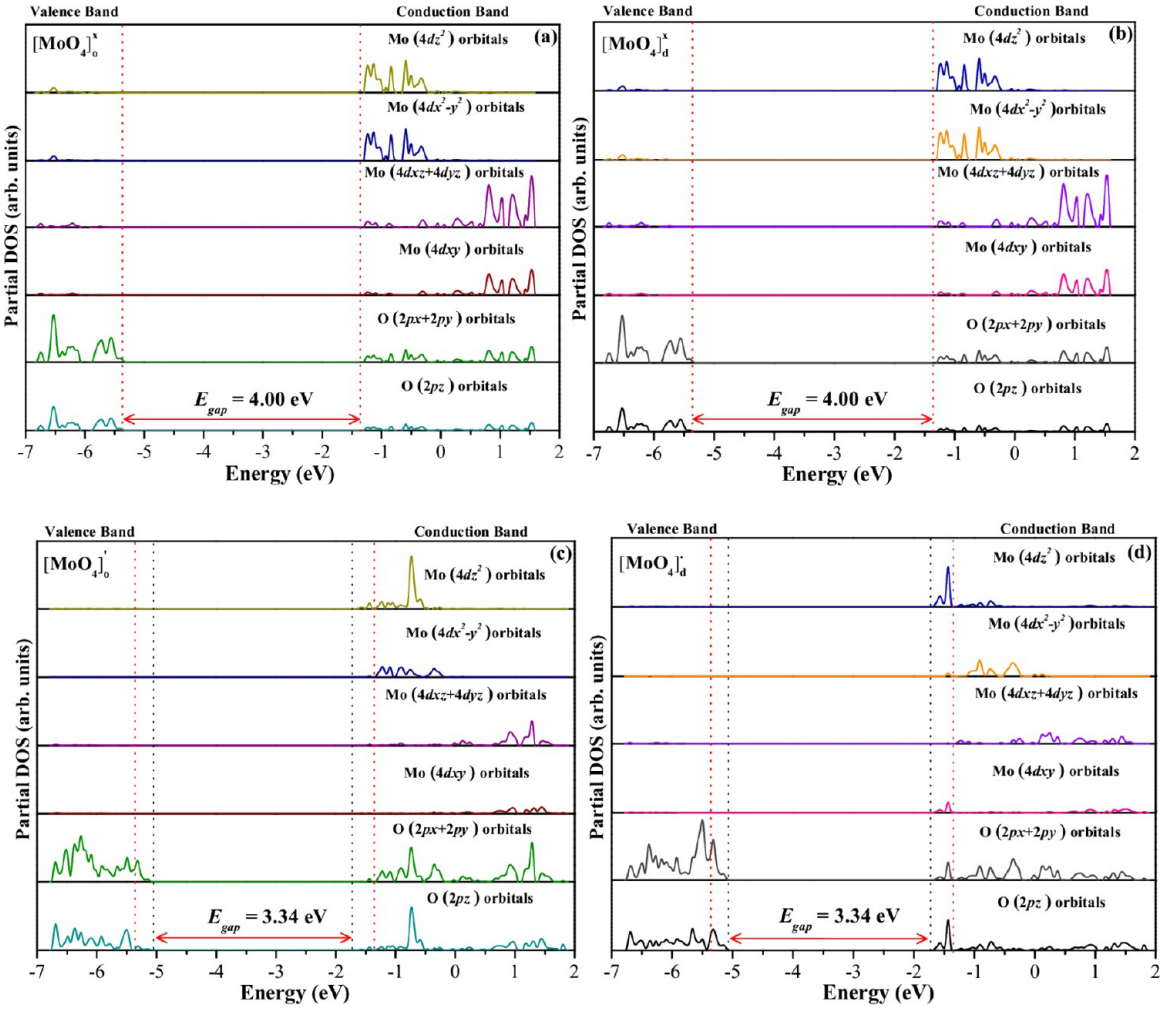

Figure 9. Partial DOS for each orbital projected to ($4d_{z^2}$ and $4d_{x^2-y^2}$ orbitals) with higher energies named (e) to Mo atom, projected ($4d_{xz}$, $4d_{yx}$, and $4d_{xy}$ orbitals) with lower energy named (t_2) to Mo atom and ($2p_x$, $2p_y$, and $2p_z$ orbitals) to O atom present in (a) ordered $[MoO_4]^x_o$ clusters and (b) disordered $[MoO_4]^x_d$ clusters both to bulk-optimized β-Ag_2MoO_4 crystals; (c) ordered $[MoO_4]_o'$ clusters and (d) disordered $[MoO_4]^{\bullet}_d$ clusters both to displacements of 0.25 Å in the Mo atoms of β-Ag_2MoO_4 crystals.

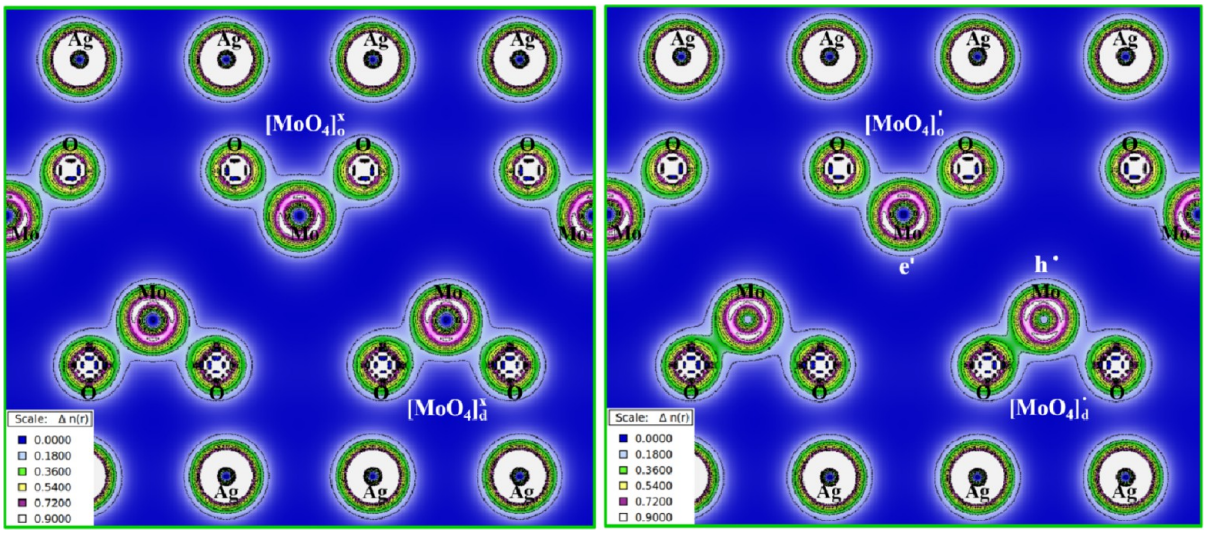

Figure 10. Electronic density map on the (101) plane with possible mechanism of charge transference between the (a) ordered $[MoO_4]^x_o$ clusters and disordered $[MoO_4]^x_d$ clusters both to bulk-optimized β-Ag_2MoO_4 crystals and (b) ordered $[MoO_4]_o'$ clusters and disordered $[MoO_4]^{\bullet}_d$ clusters both to displacements of 0.25 Å in the Mo atoms of β-Ag_2MoO_4 crystals.

dx.doi.org/10.1021/ic500335x | Inorg. Chem. 2014, 53, 5589−5599

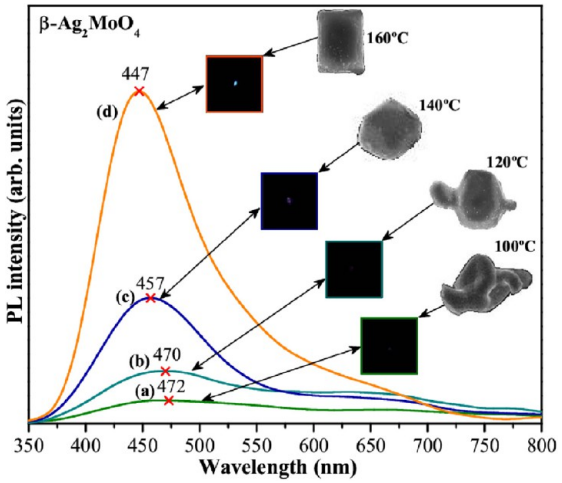

Figure 11. PL emission spectra for β-Ag_2MoO_4 microcrystals processed at different temperatures: (a) 100 °C, (b) 120 °C, (c) 140 °C, (d) 160 °C for 1 h. (insert) The shape and morphology of each individual crystal.

producing defects in the crystals. In another study,[25] the PL properties of Ag_2MoO_4 crystals were attributed to charge-transfer transitions in the anion molecular complex. However, in our previous research[57,58] on molybdates, we explained that their PL properties are related to distortions on tetrahedral $[MoO_4]$ clusters. Moreover, according the literature,[59,60] oxygen vacancies and surface defects play an important role in the visible emission. Therefore, for the β-Ag_2MoO_4 microcrystals, we believe that these distortions also reside on the octahedral $[AgO_6]$ clusters, mainly on the distorted tetrahedral $[MoO_4]$ clusters, according to our theoretical calculations.

Figure 11a–d depicts the detection of a dependence of PL spectra on the MAH processing temperature. In this particular case, there is a shift to lower wavelengths as well as an increase in PL intensity with temperature evolution. In addition to distortions on both $[AgO_6]$ and $[MoO_4]$ clusters, morphology modifications can be considered other key factors responsible for the modifications in the emission profiles of this optical property.

A charge transfer between $[AgO_6]_o^x - [AgO_6]_d^x$ and/or $[MoO_4]_o^x - [MoO_4]_d^x$ clusters due to effects of structural order–disorder in our model for the PL emissions of β-Ag_2MoO_4 crystals was considered, and it is represented in eqs 7 and 8:

$$[MoO_4]_o^x + [MoO_4]_d^x \Rightarrow [MoO_4]_o' + [MoO_4]_d^\bullet \quad (7)$$

$$[AgO_6]_o^x + [AgO_6]_d^x \Rightarrow [AgO_6]_o^x + [AgO_6]_d^\bullet \quad (8)$$

In eq (7), the cluster-to-cluster charge transfer (CCCT) in a crystal containing more than one kind of cluster is characterized by main excitations involving electronic transitions and recombination processes between clusters;[61] however, the CCCT mechanism is not detected between $[AgO_6]$ clusters (see eq 8). A study reported in the literature[62] for $CaWO_4$ crystals demonstrated that the CCCT mechanism at excited states (singlet and excited triplet states) has a significant effect on electronic transitions involved in PL emissions. Therefore, in our case, we consider that inside the disordered β-Ag_2MoO_4 microcrystals, holes ($^\bullet$) in tetrahedral $[MoO_4]_d^\bullet$ clusters and electrons (e′) in tetrahedral $[MoO_4]_o'$ clusters arise from structural distortions in the cubic structure, where the occurrence of permanent polarization and electronic transference between them is possible.[63] This conclusion is in good agreement with theoretical calculations described in Figures 8–10.

4. CONCLUSIONS

In summary, β-Ag_2MoO_4 microcrystals were synthesized by the MAH method at different temperatures (from 100 to 160 °C) for 1 h. Independent of the processing temperature, sharp diffraction peaks and well-defined Raman-active modes confirmed that this oxide is structurally ordered at long and short ranges, respectively. According to Rietveld refinement data, β-Ag_2MoO_4 microcrystals have a spinel-type cubic structure, which is composed of distorted octahedral $[AgO_6]$ and tetrahedral $[MoO_4]$ clusters. FE-SEM images revealed the occurrence of a mass transport between the particles in contact at temperatures of 120 and 140 °C. However, ideal thermodynamic conditions for the growth of cube-shaped crystals were verified only at 160 °C. The increase in the E_{gap} values with temperature evolution is explained by the reduction of intermediary energy levels between the VB and CB. Theoretical calculations indicate that band structures of all β-Ag_2MoO_4 crystals are characterized by indirect electronic transitions. According to DOS analyses, energy states in the VB are mainly constituted of 2p ($2p_x + 2p_y + 2p_z$) orbitals, while the CB is composed of Mo 4d ($4d_{z^2} + 4d_{x^2-y^2}$; $4d_{xz} + 4d_{yz} + 4d_{xy}$) orbitals. However, the contribution of Ag 6s orbitals in the CB was found in the β-Ag_2MoO_4 models with defects induced by the displacement of 0.25 Å on Ag and Mo atoms. Modifications in the PL behavior were mainly attributed to the order–disorder phenomenon caused by $[MoO_4]$ clusters in the β-Ag_2MoO_4 structure as well as morphological changes induced by temperature processing in the MAH system.

■ ASSOCIATED CONTENT

Ⓢ Supporting Information

Rietveld refinement plot of β-Ag_2MoO_4 microcrystals processed at 120, 140, and 160 °C. Lattice parameters, unit cell volumes, and atomic coordinates obtained experimentally from the structural refinement by the Rietveld method for β-Ag_2MoO_4 microcrystals processed at 120, 140, and 160 °C. Schematic representation of the paths through the Brillouin zone for a primitive cubic structure. Partial and total DOS for both (a) β-Ag_2MoO_4_Ag and (b) β-Ag_2MoO_4_Ag/Mo models. This material is available free of charge via the Internet at http://pubs.acs.org.

■ AUTHOR INFORMATION

Corresponding Author

*Tel: +55 86 3351 9308; Fax: +55 16 3351 8214. E-mail: laeciosc@bol.com.br.

Notes

The authors declare no competing financial interest.

■ ACKNOWLEDGMENTS

The Brazilian authors acknowledge the financial support of the Brazilian research financing institutions: CNPq (350711/2012-7; 479644/2012-8), CNPq-GERATEC (555684/2009-1), FAPESP (2012/07967-1; 2012/14004-5; 2012/14004-5), and CAPES.

■ REFERENCES

(1) Wenda, E. *J. Therm. Anal. Calorim.* **1990**, *36*, 1417.
(2) Wenda, E. *J. Therm. Anal. Calorim.* **1998**, *53*, 861.
(3) Suthanthiraraj, S. A.; Premchand, Y. D. *Ionics* **2004**, *10*, 254.
(4) Rocca, F.; Kuzmin, A.; Mustarelli, P.; Tomasi, C.; Magistris, A. *Solid State Ionics* **1999**, *121*, 189.
(5) Brown, S.; Marshall, A.; Hirst, P. *Mater. Sci. Eng., A* **1993**, *173*, 23.
(6) Sun, Y.; Li, C.; Zhang, Z.; Ma, X.; Wang, L.; Wang, Y.; Song, M.; Ma, P.; Jiang, L.; Guo, Y. *Solid State Sci.* **2012**, *14*, 219.

(7) Cavalcante, L. S.; Sczancoski, J. C.; Batista, N. C.; Longo, E.; Varela, J. A.; Orlandi, M. O. *Adv. Powder Technol.* **2013**, *24*, 344.
(8) Rao, K. S.; Vaidya, V. G. *Analyst* **1975**, *100*, 512.
(9) Ricci, J. E.; Linke, W. F. *J. Am. Chem. Soc.* **1951**, *73*, 3601.
(10) Cui, X.; Yu, S. H.; Li, L.; Biao, L.; Li, H.; Mo, M.; Liu, X. M. *Chem.—Eur. J.* **2004**, *10*, 218.
(11) Singh, D. P.; Sirota, B.; Talpatra, S.; Kohli, P.; Rebholz, C.; Aouadi, S. M. *J. Nanopart. Res.* **2012**, *14*, 781.
(12) Li, Z. Q.; Chen, X. T.; Xue, Z. L. *Sci. China: Chem.* **2013**, *56*, 443.
(13) Tian, G.; Sun, S. *Cryst. Res. Technol.* **2011**, *46*, 389.
(14) Tawde, D.; Srinivas, M.; Murthy, K. V. R. *Phys. Status Solidi A* **2011**, *208*, 803.
(15) Tian, Y.; Hua, G.; Xu, W.; Li, N.; Fang, M.; Zhang, L. *J. Alloys Compd.* **2011**, *509*, 724.
(16) Siqueira, K. P. F.; Moreira, R. L.; Valadares, M.; Dias, A. *J. Mater. Sci.* **2010**, *45*, 6083.
(17) Guoqiang, T.; Yuqin, Z.; Ao, X.; Yan, W.; Wei, Z. *J. Chin. Ceram. Soc.* **2011**, *39*, 43.
(18) Lei, F.; Yan, B.; Chen, H. H.; Zhang, Q.; Zhao, J. T. *Cryst. Growth Des.* **2009**, *9*, 3730.
(19) Somiya, S.; Roy, S. *Bull. Mater. Sci.* **2000**, *23*, 453.
(20) Komarneni, S.; Roy, R.; Li, Q. H. *Mater. Res. Bull.* **1992**, *27*, 1393.
(21) Mazzo, T. M.; Moreira, M. L.; Pinatti, I. M.; Picon, F. C.; Leite, F. C.; Rosa, I. L. V.; Varela, J. A.; Perazolli, L. A.; Longo, E. *Opt. Mater.* **2010**, *32*, 990.
(22) Saito, K.; Kazama, S.; Matsubara, K.; Yui, T.; Yagi, M. *Inorg. Chem.* **2013**, *52*, 8297.
(23) Hashim, M.; Hu, C.; Chen, Y.; Zhang, C.; Xi, Y.; Xu, J. *Phys. Status Solidi A* **2011**, *208*, 1937.
(24) Arora, A. K.; Nithya, R.; Misra, S.; Yagi, T. *J. Solid State Chem.* **2013**, *196*, 391.
(25) Fodjo, E. K.; Li, D. W.; Marius, N. P.; Albert, T.; Long, Y. T. *J. Mater. Chem. A* **2013**, *1*, 2558.
(26) Liu, E.; Gao, Y.; Jia, J.; Bai, Y. *Tribol. Lett.* **2013**, *50*, 313.
(27) Bish, D. L.; Post, J. E. *Am. Mineral.* **1993**, *78*, 932.
(28) MAUD http://www.ing.unitn.it/~maud/.
(29) Lutterotti, L.; Matthies, S.; Chateigner, D.; Ferrari, S.; Ricote, J. *Mater. Sci. Forum.* **2002**, *408*, 1603.
(30) Lutterotti, L.; Matthies, S.; Wenk, H. R. *IUCr—CPD Newsletter* **1999**, *21*, 14.
(31) Dovesi, R.; Saunders, V. R.; Roetti, C.; Orlando, R.; Zicovich-Wilson, C. M.; Pascale, F.; Civalleri, B.; Doll, K.; Harrison, N. M.; Bush, I. J.; D'Arco, P.; Llunell, M. *Crystal09 User's Manual;* University of Torino: Torino, Italy, 2009.
(32) Becke, A. D. *J. Chem. Phys.* **1993**, *98*, 5648.
(33) Lee, C. T.; Yang, W. T.; Parr, R. G. *Phys. Rev. B* **1988**, *37*, 785.
(34) Crystal http://www.crystal.unito.it/Basis_Sets/Ptable.html.
(35) Hay, P. J.; Wadt, W. R. *J. Chem. Phys.* **1985**, *82*, 270.
(36) Mike Towler's Crystal http://www.tcm.phy.cam.ac.uk/~mdt26/crystal.html.
(37) Wyckoff, R. W. G. *J. Am. Chem. Soc.* **1922**, *44*, 1994.
(38) Kunert, H. W. *J. Phys.: Conf. Ser.* **2006**, *30*, 290.
(39) Wang, P.; Huang, B.; Qin, X.; Zhang, X.; Dai, Y.; Whangbo, M. H. *Inorg. Chem.* **2009**, *48*, 10697.
(40) Lin, J.; Wang, Q.; Zheng, Y.; Zhang, Y. *CrystEngComm* **2013**, *15*, 5668.
(41) Kotova, I. Y.; Korsun, V. P. *Russ. J. Inorg. Chem.* **2010**, *55*, 1965.
(42) Bao, Z. Y.; Lei, D. Y.; Dai, Y.; Wu, Y. *Appl. Surf. Sci.* **2013**, *287*, 404.
(43) Rietveld, H. M. *Acta Crystallogr.* **1967**, *22*, 151.
(44) Momma, K.; Izumi, F. *J. Appl. Crystallogr.* **2011**, *44*, 1272.
(45) Available at: <http://en.wikipedia.org/wiki/Octahedron>.
(46) Available at: <http://en.wikipedia.org/wiki/Tetrahedron>.
(47) Beltrán, A.; Gracia, L.; Longo, E.; Andrés, J. *J. Phys. Chem. C* **2014**, *118*, 3724.
(48) Liu, E. Y.; Wang, W. Z.; Gao, Y. M.; Jia, J. H. *Tribol. Lett.* **2012**, *47*, 21.
(49) Marques, V. S.; Cavalcante, L. S.; Sczancoski, J. C.; Alcântara, A. F. P.; Orlandi, M. O.; Moraes, E.; Longo, E.; Varela, J. A.; Siu Li, M.; Santos, M. R. M. C. *Cryst. Growth Des.* **2010**, *10*, 4752.
(50) Bomio, M. R. D.; Cavalcante, L. S.; Almeida, M. A. P.; Tranquilin, R. L.; Batista, N. C.; Pizani, P. S.; M. Siu Li, M. S.; Andres, J.; Longo, E. *Polyhedron* **2013**, *50*, 532.
(51) Kubelka, P.; Munk-Aussig, F. *Z. Tech. Phys.* **1931**, *12*, 593.
(52) Morales, A. E.; Mora, E. S.; Pal, U. *Rev. Mex. Fis. S* **2007**, *53*, 18.
(53) Smith, R. A. *Semiconductors,* 2nd ed.; Cambridge University Press: London, U.K., 1978; p 434.
(54) Lacomba-Perales, R.; Ruiz-Fuertes, J.; Errandonea, D.; Martínez-García, D.; Segura, A. *EPL* **2008**, *83*, 37002.
(55) Cavalcante, L. S.; Almeida, M. A. P.; Avansi, W.; Tranquilin, R. L.; Longo, E.; Batista, N. C.; Mastelaro, V. R.; Li, M. S. *Inorg. Chem.* **2012**, *51*, 10675.
(56) Cavalcante, L. S.; Moraes, E.; Almeida, M. A. P.; Dalmaschio, C. J.; Batista, N. C.; Varela, J. A.; Longo, E.; Li, M. S.; Andrés, J.; Beltrán, A. *Polyhedron* **2013**, *54*, 13.
(57) Sczancoski, J. C.; Cavalcante, L. S.; Marana, N. L.; da Silva, R. O.; Tranquilin, R. L.; Joya, M. R.; Pizani, P. S.; Varela, J. A.; Sambrano, J. R.; Li, M. S.; Longo, M. S.; Andrés, J. *J. Curr. Appl. Phys.* **2010**, *10*, 614.
(58) Sczancoski, J. C.; Bomio, M. D. R.; Cavalcante, L. S.; Joya, M. R.; Pizani, P. S.; Varela, J. A.; Longo, E.; Li, M. S.; Andres, J. A. *J. Phys. Chem. C* **2009**, *113*, 5812.
(59) Fang, Y. P.; Xu, Y. P.; Dong, W. F. *Small* **2005**, *10*, 967.
(60) Shi, H. Y.; Deng, B.; Zhong, S. L.; Wang, S. L.; Xu, A. W. *J. Mater. Chem.* **2011**, *21*, 12309.
(61) Cavalcante, L. S.; Longo, V. M.; Sczancoski, J. C.; Almeida, M. A. P.; Batista, A. A.; Varela, J. A.; Orlandi, M. O.; Longo, E.; Li, M. S. *CrystEngComm* **2012**, *14*, 853.
(62) Gracia, L.; Longo, V. M.; Cavalcante, L. S.; Beltran, A.; Avansi, W.; Li, M. S.; Mastelaro, V. R.; Varela, J. A.; Longo, E.; Andres, J. *J. Appl. Phys.* **2011**, *110*, 043501.
(63) Cavalcante, L. S.; Sczancoski, J. C.; Li, M. S.; Longo, E.; Varela, J. A. *Colloids Surf., A* **2012**, *396*, 346.